Available online at www.sciencedirect.com

ScienceDirect

Advances in Space Research 74 (2024) 3045–3059

ADVANCES IN SPACE RESEARCH (a COSPAR publication)

www.elsevier.com/locate/asr

Antenna and attitude modeling of modernized GLONASS satellites

Peter Steigenberger [a,*], Oliver Montenbruck [a], André Hauschild [b]

[a] Deutsches Zentrum für Luft- und Raumfahrt (DLR), German Space Operations Center (GSOC), Münchener Straße 20, 82234 Weßling, Germany
[b] Deutsches Zentrum für Luft- und Raumfahrt (DLR), Institute of Communications and Navigation (IKN), Münchener Straße 20, 82234 Weßling, Germany

Received 8 May 2024; received in revised form 28 June 2024; accepted 1 July 2024
Available online 6 July 2024

Abstract

Next to the legacy frequency division multiple access (FDMA) signals in the L1 and L2 band, modernized GLONASS satellites of the M+, K1, and K2 generation also transmit new code division multiple access (CDMA) signals on L3, and, in part, the L1 and L2 frequencies. Depending on the specific satellite platform, either a common antenna or two distinct antennas are used for the individual signals. As a novel feature, the new CDMA navigation messages provide information on the antenna phase center locations as well as the spacecraft orientation during rate-limited noon and midnight turns. We establish a comprehensive set of phase center positions for the individual GLONASS antennas from manufacturer data and information in the CDMA navigation messages, inferred from the comparison of FDMA and CDMA broadcast ephemerides, and obtained from antenna baseline estimates using a triple-frequency carrier phase combination. Based on these, reference values for the signal-specific PCOs of each block of modernized GLONASS spacecraft are derived that may be used to extend the current antenna model of the International GNSS Service (IGS) to all frequency bands. Complementary to the analysis of antenna phase center information, the new CDMA attitude model for GLONASS-K satellites is reviewed. Algorithms for computing relevant parameters of the rate-limited yaw slews including the ramp-up and -down phase based on the Sun/orbit geometry are derived that enable a concise attitude modeling in GLONASS orbit determination and precise point positioning. The model is validated through comparison with yaw angle estimates derived from triple-frequency observations showing consistency at the 1° level for the K2 satellite. On the other hand, unexpected accelerations during noon turns of GLONASS-M+ are identified, which may cause short-term yaw angle deviations of up to 20° relative to attitude models in common use within the IGS.

Keywords: GLONASS-M+; GLONASS-K; CDMA; L3; Navigation message; Phase center

1. Introduction

GLONASS satellites traditionally transmit frequency division multiple access (FDMA) signals in the L1 (1598.0625–1605.3750 MHz) and L2 (1242.9375–1248.6250 MHz) frequency bands (RISDE, 2008). Starting with the first GLONASS-K1 satellite, a code division multiple access (CDMA) open service signal (L3OC) on the L3 frequency (1202.025 MHz) was introduced in 2011 (Russian Space Systems, 2016c). CDMA signals in the L2 frequency band (L2OC; 1248.06 MHz; Russian Space Systems, 2016b) and in the L1 frequency band (L1OC; 1600.995 MHz; Russian Space Systems, 2016a) were added with space vehicle number (SVN) R807 and R803 in 2022 and 2023, respectively. An overview of GLONASS satellites with CDMA signal capability is provided in Table 1.

The R801 satellite transmits the L3 CDMA signals via a dedicated antenna (Montenbruck et al., 2015), whereas all other K1 satellites use the same antenna for L1/L2 FDMA and L3 CDMA signals. In order to distinguish these different satellite types, they are labeled as GLONASS-K1A and -K1B, respectively. Similar to K1A, the GLONASS-M+ spacecraft also transmit the L3 CDMA signal from a

* Corresponding author.
E-mail address: peter.steigenberger@dlr.de (P. Steigenberger).

https://doi.org/10.1016/j.asr.2024.07.001
0273-1177/

Table 1
GLONASS satellites supporting CDMA signals. SVN denotes the space vehicle number as used by the International GNSS Service (IGS). These numbers differ by 100 from those used by the system provider for newer satellites in order to get unique SVNs (Steigenberger and Montenbruck, 2022). Furthermore, the orbital slot and pseudo-random noise (PRN) numbers assigned in early 2024 are given.

SVN	Slot	Type	launched	CDMA signals	Notes
	(PRN)				
R801		K1A	2011/02/26	L3OC	until Oct. 2020
R802	R09	K1B	2014/11/30	L3OC	ICD 2011
R803	R26	K2	2023/08/07	L3OC, L2OC, L1OC	
R805	R11	K1B	2020/10/25	L3OC	
R806	R22	K1B	2022/07/07	L3OC	
R807	R25	K1B	2022/10/10	L3OC, L2OC	
R855	R21	M+	2014/06/14	L3OC	
R856	R05	M+	2018/06/16	L3OC	
R858	R12	M+	2019/05/27	L3OC	
R859	R04	M+	2019/12/11	L3OC	
R860	R24	M+	2020/03/16	L3OC	
R861	R16	M+	2022/11/28	L3OC	

separate antenna. R803 is the first GLONASS-K2 satellite and supports CDMA signals in all three frequency bands (Thoelert et al., 2024). It makes use of two distinct antennas for transmission of the CDMA and FDMA signals (Fig. 1). Use of separate antennas for individual sets of signals enables transmission of all signals at a constant power envelope without requiring advanced modulation techniques.

Within this work, we investigate the frequency-specific phase center locations of the individual GLONASS-M+, -K1, and -K2 antennas. Following an overview of the FDMA and CDMA navigation messages in Section 2, a summary of previously disclosed manufacturer information and metadata in the CDMA navigation messages is provided, and an independent analysis of triple-frequency carrier phase observations is presented in Section 3. Complementary to the determination of phase center offsets (PCOs), the new GLONASS-K attitude model for rate-limited noon and midnight turns is discussed in Section 4. Based on L1/L2/L3 observations of the first K2 satellite, the consistency of the actual yaw profile with the newly introduced CDMA attitude parameters is assessed.

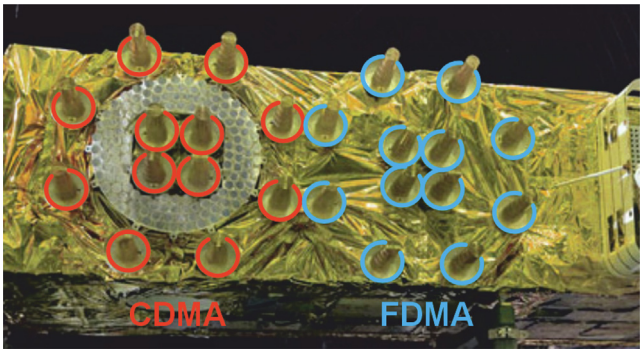

Fig. 1. Antenna panel of the first GLONASS-K2 satellite showing the CDMA antenna (left; red; with embedded laser retroreflector array) and the FDMA antenna (right; blue). Image credit: ISS Reshetnev.

We acknowledge that related results from a concurrent study have recently been released by Dilssner and Springer (2024), who conducted a first analysis of GLONASS-K1A and -K2 yaw maneuvers based on triple-carrier observation. Our contribution complements and extends their analysis with a more rigorous application of this technique and a critical discussion of its limitations. Next to comparing observed yaw angles with the theoretical model of rate-limited yaw maneuvers, we evaluate the quality of the CDMA phase center information and attitude parameters and provide recommendations for updating antenna and attitude models within the International GNSS Service (IGS; Johnston et al., 2017).

2. GLONASS navigation messages

Orbit and clock information for use with tracking of the open service FDMA signals (L1OF, L2OF) is provided in a corresponding navigation message (RISDE, 2008) that is jointly modulated on the respective carrier along with the coarse/acquisition (C/A) ranging code. In accord with the nomenclature of the Receiver INdependent EXchange (RINEX; Gini, 2023) format, it is here denoted as FDMA navigation message. While a separate navigation message with different content is transmitted with the FDMA P-code, it lacks a public specification and will not further be considered in this study. Based on investigations of Daly and Riley (1994), the P-code message uses a different layout, but provides similar information with a four-times higher numerical resolution. New types of navigation data with a more flexible message scheme were introduced as part of the new CDMA signals (Povalyaev, 2013). Here, independent broadcast ephemerides for users of the L1 and L3 open service CDMA signals are provided in the L1OC and L3OC navigation messages (Russian Space Systems, 2016a; Russian Space Systems, 2016c), while the L2 CDMA signal provides a currently non-disclosed "channel for service information" (CSI) data message (Russian Space Systems, 2016b).

The FDMA navigation message (RISDE, 2008; Daly and Riley, 1994) is made up of superframes with 150 s duration consisting of five frames, see Fig. 2. Each superframe contains a set of "immediate data" with the orbit and clock information of the transmitting satellite as well as the almanac of 24 GLONASS satellites. Individual frames are divided into 15 strings of 100 bits and 2 s duration. Out of these, four strings provide data for the transmitting satellite. The fifth string contains system time offsets (GLONASS/UTC(SU) and GPS/GLONASS), while the remaining strings provide the almanac of four to five GLONASS satellites. The fifth frame contains only almanac data of four satellites but also the coefficients B1 and B2 of a linear polynomial modeling the difference between UT1 and UTC(SU) as well as a leap second flag KP. GLONASS orbit data in the FDMA navigation message are provided in the form of state vectors in an Earth-fixed reference frame, which need to be numerically integrated from the reference epoch to the epoch of interest (Deshpande et al., 2011). Conceptually, the state vectors as well as the resulting positions are referred to an antenna phase center of unspecified nature, but can be used directly with the associated satellite clock offset information to obtain modeled pseudoranges inside a GLONASS receiver.

CDMA navigation messages with similar content but a different layout are part of the L3OC signal transmitted by GLONASS-M+, -K1, and -K2 satellites as well as the L1OC signal, which is currently only supported by the new K2 spacecraft (Fig. 2). Other than the frame-oriented design of the FDMA navigation message with its static arrangement of the individual data, a message concept similar to the GPS CNAV navigation message (Steigenberger et al., 2015) is adopted in the GLONASS CDMA navigation messages, which offers a higher flexibility concerning the information content, granularity and update rate of individual parameters.

A preliminary definition of individual messages, termed "strings" for the L3OC signal was released along with the launch of the first K1 satellite (Russian Space Systems, 2011). It comprises a total of five messages for orbit, clock, accuracy, and system time data (strings 1–3), as well as almanac, ionosphere, and leap-second data (strings 4–5). The 2011 L3OC signal definition was initially used on all GLONASS-M+ and -K1 satellites and is still used by the second K1 satellite, R802. At an unknown time between 2020 and 2023, all other satellites were updated to the new CDMA interface control documents (ICDs) released in 2016 (Russian Space Systems, 2016a; Russian Space

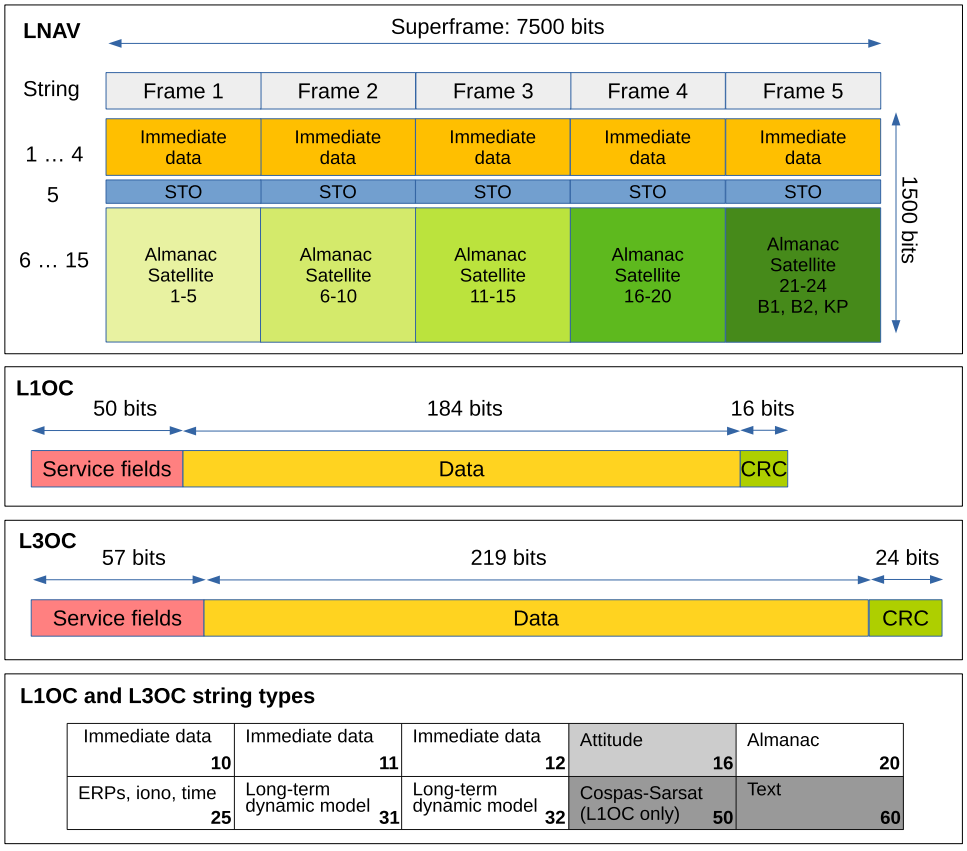

Fig. 2. Structure of GLONASS FDMA and CDMA navigation messages. CRC: cyclic redundancy check; STO: system time offsets. B1 and B2 describe the difference between UT1 and UTC(SU). KP is a leap second flag. String types shaded in gray are transmitted only on a per-needed basis, while white indicates strings that are currently transmitted at regular intervals.

Systems, 2016b; Russian Space Systems, 2016c) without public notice.

The string layout and content of the 2016 ICD L1OC and L3OC navigation messages is illustrated in Fig. 2. The L3OC CDMA navigation strings exhibit a nominal length of 300 bits, which includes a service field of 57 bits with timing information and a cyclic redundancy check (CRC) field of 24 bits. At a data rate of 100 bps, a complete string is transmitted in 3 s. A slightly different length of 250 bits with a 50-bit service field and a 16-bit CRC are adopted for the L1OC message, which is transmitted in 2 s at a rate of 250 bps. Both L3OC and L1OC navigation data comprise a set of currently 9 predefined string types for ephemeris data and auxiliary information. Similar to the FDMA message, the "immediate data" (strings 10–12) provide the key ephemeris information (orbit, clock, accuracy, group delays) required for real-time positioning. In addition, phase center information and system time offsets are provided in these strings. Next to the almanac data (string 20) covering the CDMA-capable satellites, dedicated strings with Earth rotation parameters (ERPs), ionosphere model parameters and leap second information (string 25), a new type of long-term dynamic model parameters (LDMP) offering orbit data with an extended 4 h validity (strings 31, 32), attitude model parameters (string 16), and a text message string (type 60) are currently defined. L1OC, furthermore, offers a distinct message type 50 for COSPAS-SARSAT (Ilcev, 2007) notices.

Within this study, specific attention is given to orbit data and phase center offsets provided in messages 10–12 as well as attitude information in message 16. The CDMA ephemeris data make use of the same orbit model as the legacy FDMA message but offer a notably higher numerical resolution (0.95 mm vs. 0.49 m). A major conceptual difference relates to the fact that CDMA orbit data refer to the position and velocity of the spacecraft center of mass, rather than an antenna phase center. Users of the CDMA navigation data are thus required to explicitly model the phase center location by accounting for the PCO in the spacecraft body frame and the spacecraft orientation in the Earth-fixed system used for the orbit, position and pseudorange modeling.

For most of the time, all GLONASS satellites follow a nominal yaw steering law (Montenbruck et al., 2015), which enables computation of their attitude based on the known Sun-spacecraft-Earth geometry. As an exception, a rate-limited yaw slew is performed during noon and midnight turns whenever the Sun is close to the orbital plane and the nominal yaw steering would require a rate exceeding the design limitations. As the first global navigation satellite system (GNSS), GLONASS provides a dedicated message (type 16) with parameters describing the yaw angle variation during such rate-limited slews. The CDMA attitude message is only transmitted by the current GLONASS-K1B and -K2 satellites during short intervals covering the noon and midnight turns near the center of the eclipse season. It enables a proper modeling of the phase center location together with the L1 and L3 CDMA antenna PCOs in the type 12 ephemeris message. Relevant algorithms for GLONASS attitude modeling during periods of nominal and rate-limited yaw steering are provided in Russian Space Systems (2016d).

GLONASS FDMA ephemeris data used in the present analysis are obtained from DLR's BRD400DLR multi-GNSS navigation data product (Montenbruck and Steigenberger, 2022) in RINEX 4 (Gini, 2023) format, which is publicly shared through data repositories of the IGS. L3OC navigation data of GLONASS-M+, -K1, and -K2 satellites as well as K2 L1OC navigation data have been extracted from raw navigation data frames collected with two JAVAD TRE-3S receivers hosted at the German Space Operations Center in Oberpfaffenhofen, Germany, and the University of New South Wales (UNSW) near Sydney, Australia, and equipped with a prototype firmware provided by the manufacturer. The respective data are archived in a proposed extension of the RINEX 4 format currently under discussion within the IGS.

3. Phase center offsets

Knowledge of the antenna phase center (APC) location is vital for a proper modeling of GNSS observations in precise positioning. It provides the link between the location of the spacecraft center-of-mass (COM), which is described by the orbital dynamics models and the point of transmission of the ranging signals. As part of the broadcast ephemeris messages, GNSS real-time navigation users are traditionally provided with APC-related orbit information that has been generated in the control center by applying the corresponding phase center offset (PCO). In contrast to this, orbit information for precise positioning users (Weiss et al., 2017) is commonly referred to the COM and complemented with applicable antenna and attitude models. For GLONASS, the igs20.atx antenna model (Rebischung et al., 2022) introduced in 2022 provides estimated z-PCOs for the ionosphere-free linear combination of L1/L2 FDMA observations of current and past GLONASS satellites that are aligned to the IGS20 reference frame (Rebischung et al., 2024).

As a contribution to extending the IGS antenna model to all signal frequencies, we summarize and compare PCO data of the active GLONASS-M+/K1/K2 satellites obtained from the manufacturer, retrieved or inferred from CDMA and FDMA navigation data, and determined from observations. Throughout this work, we refer all PCOs to the spacecraft body frame, making use of IGS axis conventions. These aim at a harmonized axis labeling across a wide range of GNSSs and satellite platforms and are based on the designation of the nadir-pointing spacecraft axis and the solar-panel rotation axis as $+z$ and $\pm y$-axes, respectively, while the positive x-axis points into the Sun-lit hemisphere during nominal yaw steering (Montenbruck et al., 2015). Starting with the GLONASS-M generation, the

IGS axis conventions are related to the GLONASS manufacturer conventions by the transformation

$$\begin{aligned} +x_{\mathrm{IGS}} &= -y_{\mathrm{GLO}} \\ +y_{\mathrm{IGS}} &= +z_{\mathrm{GLO}} \\ +z_{\mathrm{IGS}} &= -x_{\mathrm{GLO}}. \end{aligned} \tag{1}$$

3.1. Manufacturer and provider data

For the GLONASS-M+ and -K1B satellites, frequency-specific PCO values have earlier been released by the spacecraft manufacturer (Fatkulin, 2015). The values were partly published in Montenbruck et al. (2015) and are reproduced in Table 2 for further discussion. Concerning the FDMA PCOs of M+ and K1B satellites, identical z-differences of 0.130 m between the L1 and L2 PCOs may be noted, which hints at the use of a common antenna design on both platform types.

Independent values of the L1OC and L3OC antenna PCOs are provided as part of the signal-in-space by M+, K1, and K2 satellites transmitting the respective CDMA navigation messages in accord with the 2016 ICD version. As of early 2024, identical PCO values are transmitted by the individual satellites within a given block. While the L3OC phase center provided in the L3OC message for GLONASS-K1B satellites agrees with the early values given in Fatkulin (2015) to better than 1 cm, a 12 cm difference can be noted for the M+ satellites.

Based on the L1 and L3 phase center offsets transmitted in the L1OC and L3OC message of the GLONASS-K2 satellite, the K2 CDMA antenna is located on the spacecraft z-axis (i.e., at $x = y = 0$ m). This is consistent with Fig. 1, which shows that the CDMA antenna is aligned with the mounting hole for the solar panel rotation axis. Furthermore, it may be noted that the 13.5 cm difference between the z-components of the L3 and L1 CDMA phase center of K2 closely matches the manufacturer values for the difference of L3 CDMA and L1 FDMA z-PCOs for the K1B satellites. This suggests a common design of the K1B and K2 antenna assemblies in agreement with publicly available images of the respective antenna arrays.

As noted earlier, orbit information in the CDMA messages refers to the COM, while FDMA ephemerides provide the location of the FDMA antenna phase center. Assuming that both ephemerides represent the same trajectory, this opens the possibility to infer the FDMA antenna PCO from the difference

$$\boldsymbol{d}_{\mathrm{FDMA}} = \boldsymbol{T}\left(\boldsymbol{r}^{\mathrm{APC}}_{\mathrm{FDMA}} - \boldsymbol{r}^{\mathrm{COM}}_{\mathrm{CDMA}}\right) \tag{2}$$

of FDMA- and CDMA-based satellite positions. Here, $\boldsymbol{T}$ denotes the transformation from the Earth-fixed reference frame of the broadcast ephemerides to the spacecraft body frame, which can be computed in accord with the CDMA attitude model for nominal and rate-limited yaw steering (Russian Space Systems, 2016d).

In practice, we obtained the antenna offsets by averaging over a sufficient number of broadcast ephemeris data sets and epochs within the ± 15 min validity period of each data set to compensate for the coarse discretization of state vectors in the FDMA message. As illustrated in Fig. 3 for a sample GLONASS-M+ satellite, the epoch-wise differences exhibit a standard deviation of $\sigma(\boldsymbol{d}_{\mathrm{FDMA}}) \approx 0.25$ m, which results in a precision of about ≈ 4 cm for daily averages and 3 mm for averages over five months as considered in this study. As an exception, slightly higher uncertainties apply for the new K2 satellite in view of a reduced availability of CDMA and FDMA ephemerides in the data analysis period.

Strictly speaking, $\boldsymbol{d}_{\mathrm{FDMA}}$ provides an estimate of the antenna offset adopted by the GLONASS control center for generating the FDMA navigation message. While the FDMA ICD (RISDE, 2008) is unspecific about the choice of a reference frequency or frequency combination for this PCO, comparison with the individual manufacturer values suggests that the FDMA PCO actually describes the offset of the L1 phase center from the COM. It is therefore listed as an L1 PCO estimate in Table 2. Differences from the L1 FDMA manufacturer values amount to roughly 1–4 cm, which partly exceed the error budget of the long-term averages, but might also relate to systematic differences in the CDMA and FDMA ephemeris generation in the control center. For the lateral position of the GLONASS-K2 FDMA antenna, the analysis yields a value of $x_{\mathrm{FDMA}} = 0.956$ m, which closely matches the FDMA − CDMA antenna offset of 0.96 m provided in an anonymous design drawing of the K2 antenna panel reproduced by Steigenberger (2023).

3.2. Triple-frequency baseline estimation

As suggested by Hauschild (2019), the baseline between phase centers of multiple transmit antennas onboard a GNSS satellite can be estimated using a linear combination

$$\varphi_{\mathrm{tri}} = \kappa_a \varphi_a + \kappa_b \varphi_b + \kappa_c \varphi_c \tag{3}$$

of carrier phases φ_a, φ_b, and φ_c on three distinct frequencies f_a, f_b, and f_c that eliminates both the common contributions to the geometric range as well as the first-order ionospheric phase advance. Triple-carrier combinations with these properties have first been discussed in Simsky (2006) with focus on multipath analysis and were later adopted for studying temperature-induced phase bias variations of GPS IIF satellites in Montenbruck et al. (2012).

The coefficients of the triple-carrier combination may be determined in a straightforward manner by considering that the difference

$$\mathrm{IF}(\varphi_a, \varphi_b) - \mathrm{IF}(\varphi_a, \varphi_c) = (\gamma_{ab} - \gamma_{ac})\varphi_a - \gamma_{ab}\varphi_b + \gamma_{ac}\varphi_c \tag{4}$$

Table 2
GLONASS phase center offsets (x, y, z) from manufacturer information, broadcast ephemerides, and triple-frequency observations. All values in [m]. Subscripts C and F denote CDMA and FDMA values, respectively. The factor κ_c is defined in Eq. 6 and amounts to roughly 0.19.

Sat. type	Band	Manufacturer	L1OC/L3OC nav msg	FDMA – CDMA	Triple-frequency
M+	$L1_F$	$(-0.545, 0.000, +2.099)$[a]		$(-0.526, -0.009, 2.061)$[b]	
	$L2_F$	$(-0.545, 0.000, +1.969)$[a]			
	$L3_C$	$(-1.100, 0.000, +2.067)$[a]	$(-1.100, 0.000, +2.191)$		
	$(L3_C - L2_F) - \kappa_c \cdot (L2_F - L1_F)$	$(-0.555, 0.000, +0.123)$[c]	$(-0.555, 0.000, +0.247)$[d]		$(-0.565, +0.003, +0.271)$[b]
K1B	$L1_F$	$(0.000, 0.000, +1.561)$[a]		$(+0.017, +0.016, +1.547)$[b]	
	$L2_F$	$(0.000, 0.000, +1.431)$[a]			
	$L3_C$	$(0.000, 0.000, +1.426)$[a]	$(-0.006, 0.000, +1.428)$		
	$(L3_C - L2_F) - \kappa_c \cdot (L2_F - L1_F)$	$(0.000, 0.000, +0.020)$[c]	$(-0.006, 0.000, +0.021)$[d]		$(-0.006, +0.002, +0.162)$[b]
K2	$L1_F$	$(+0.960, 0.000,$ n/a$)$[e]	$(+0.960, +0.000, +0.975)$[f]	$(+0.956, +0.001, +0.946)$[g]	
	$L2_F$	$(+0.960, 0.000,$ n/a$)$[e]	$(+0.960, +0.000, +0.844)$[f]		
	$L1_C$		$(0.000, 0.000, +0.975)$		
	$L2_C$		$(0.000, 0.000, +0.844)$[h]		
	$L3_C$		$(0.000, 0.000, +0.840)$		
	$(L3_C - L2_F) - \kappa_c \cdot (L2_F - L1_F)$		$(-0.960, 0.000, +0.018)$[c]		$(-0.955, -0.006, -0.068)$[g]

[a] Fatkulin (2015)
[b] Block-mean estimates; see text for discussion of expected uncertainty
[c] Computed values
[d] Computed from $L1_F/L2_F$ manufacturer and $L3_C$ navigation message values
[e] Steigenberger (2023)
[f] x/y-PCOs from manufacturer; assuming identical L1 and L2 z-PCOs of FDMA and CDMA antennas
[g] Single-satellite estimates; see text for discussion of expected uncertainty
[h] Assuming identical L3 − L2 PCO differences for K2 and K1B antennas

of two pairs of ionosphere-free dual-frequency linear combinations with

$$\gamma_{ab} = \frac{f_b^2}{f_a^2 - f_b^2} \quad \text{and} \quad \gamma_{ac} = \frac{f_c^2}{f_a^2 - f_c^2}, \tag{5}$$

exhibits the desired properties of being both ionosphere- and geometry-free. Obviously, these properties are retained when scaling all coefficients with a common factor, which allows for different, application-dependent normalizations.

For estimating the baseline between the L3 CDMA phase center and the phase center(s) of the L1/L2 FDMA antenna of a GLONASS-M+, -K1, or -K2 satellite, we identify indices a, b, and c with L3 CDMA, L2 FDMA, and L1 FDMA observations, respectively. Furthermore, we adopt the scaled coefficients

$$\kappa_a = 1, \quad \kappa_b = -(1 + \kappa_c), \quad \kappa_c = \frac{\gamma_{ac}}{\gamma_{ab} - \gamma_{ac}} \tag{6}$$

of a triple-carrier combination with a unit value of κ_a that are obtained upon dividing Eq. (4) by $\gamma_{ab} - \gamma_{ac}$. The numerical values of these coefficients depend on the frequency channel number of the FDMA signal and range from $\kappa_c \approx 0.18$ for $k = -7$ to $\kappa_c \approx 0.20$ for $k = +6$.

Building on the observation model for individual observations (Hauschild, 2017) and linearizing the transmitter-to-receiver range relative to the center-of-mass, the observation model for the triple-carrier combination of carrier phase ranges is obtained as

$$\varphi_{\text{tri}} = \boldsymbol{e}^T \boldsymbol{R}_z(\psi)^T \boldsymbol{d}_{\text{tri}} + A_{\text{tri}} + \xi^{\text{s}}_{\text{tri}} + \xi^{\text{r}}_{\text{tri}} + \frac{\lambda_{\text{tri}}}{2\pi} \Psi + b_{\text{tri}} + \varepsilon_{\text{tri}}. \tag{7}$$

Here, $\boldsymbol{e}$ is the receiver-to-satellite line-of-sight unit vector expressed in the Earth-fixed reference frame used to describe the satellite position. $\boldsymbol{R}_z(\psi)$ denotes a rotation around the spacecraft z-axis with the yaw angle ψ and represents the transformation from Earth-fixed coordinates to the spacecraft body frame. The vector

$$\begin{aligned} \boldsymbol{d}_{\text{tri}} &= \boldsymbol{d}_{\text{L3C}} - (1 + \kappa_c) \cdot \boldsymbol{d}_{\text{L2F}} + \kappa_c \cdot \boldsymbol{d}_{\text{L1F}} \\ &= (\boldsymbol{d}_{\text{L3C}} - \boldsymbol{d}_{\text{L2F}}) - \kappa_c \cdot (\boldsymbol{d}_{\text{L2F}} - \boldsymbol{d}_{\text{L1F}}) \end{aligned} \tag{8}$$

is the triple-frequency combination of the antenna- and frequency-specific PCOs $\boldsymbol{d}_i$ expressed in the spacecraft body frame. A_{tri} and b_{tri} denote the triple-frequency combinations of the individual carrier phase ambiguities and possible time-varying carrier phase biases, respectively. The remaining terms describe the respective contributions of satellite and receiver antenna phase patterns $(\xi^{\text{s}}_{\text{tri}}, \xi^{\text{r}}_{\text{tri}})$, phase wind-up (with wavelength λ_{tri} and relative antenna rotation angle Ψ), as well as noise and unmodeled errors $(\varepsilon_{\text{tri}})$.

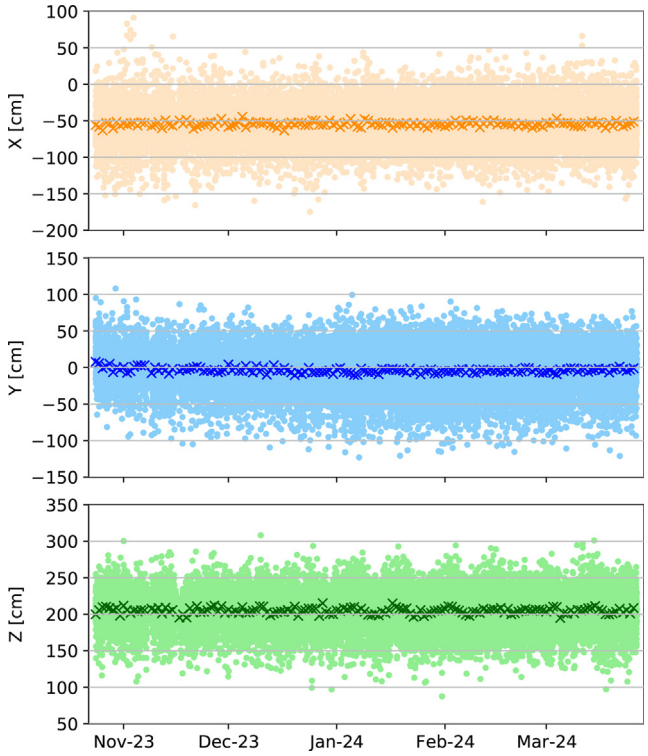

Fig. 3. PCO estimates of the GLONASS-M+ satellite R858 from differences of FDMA and CDMA ephemerides. Colored dots indicate epoch-wise values at 5-min sampling, while daily averages are marked by crosses.

Initial analysis showed pronounced systematic effects in the baseline estimates, which can be attributed to time-dependent satellite biases. Thus, a periodic model

$$b_{\mathrm{tri}} = \sum_{i=1}^{n} (b_{c,i}\cos(i\mu) + b_{s,i}\sin(i\mu)) \tag{9}$$

as suggested by Montenbruck et al. (2012) for the GPS IIF satellites is adopted for the present study. Here, the temporal variation is described in terms of harmonics up to degree n of the orbit angle μ counted from local midnight. In practice, orbit-periodic biases can be adequately described with a model of degree $n = 3$. This model implicitly satisfies a zero-mean condition $\overline{b_{\mathrm{tri}}(t)} = 0$ over time t, which is adopted to avoid a singularity in the observation model. The constant part of the bias is thus lumped into the phase ambiguities.

Using triple-frequency carrier phase observations from a sufficiently large and dense station network, the "baseline" vector $\boldsymbol{d}_{\mathrm{tri}}$, which actually represents a linear combination of three PCOs, can be determined in a least-squares adjustment along with a vector of ambiguities for the set of continuous carrier tracking arcs and the optional harmonic bias coefficients. For our analysis of GLONASS-M+, -K1, and -K2 satellites, we considered a set of up to 158 stations from the IGS multi-GNSS network (Johnston et al., 2017), the Plate Boundary Observatory (UNAVCO Community, 2004, 2006, 2007a,b,c), and SuomiNet (UNAVCO Community, 2007d) supporting GLONASS L1, L2, and L3 observations. Subject to availability, a maximum data interval from January 2023 to March 2024 was considered. In the case of GLONASS-K2, observations are restricted to a 6.5 months period starting in the middle of September 2023 and a maximum of about 85 stations.

For computation of the yaw angle ψ in Eq. (7), a nominal yaw steering (Bar-Sever, 1996; Montenbruck et al., 2015) applies for the vast majority of epochs. For periods with rapid noon and midnight turns, rate-limited yaw models of Dilssner et al. (2011) and Russian Space Systems (2016d) were used, which are further described in Section 4. Receiver antenna patterns were modeled based on the igs20.atx antenna model (Rebischung et al., 2022) and phase wind-up was described based on the model of Wu et al. (1993). It may be noted, though, that the effective wavelength

$$\begin{aligned}\lambda_{\mathrm{tri}} &= \kappa_a\lambda_a + \kappa_b\lambda_b + \kappa_c\lambda_c \\ &= (\lambda_{\mathrm{L3C}} - \lambda_{\mathrm{L2F}}) - \kappa_c \cdot (\lambda_{\mathrm{L2F}} - \lambda_{\mathrm{L1F}})\end{aligned} \tag{10}$$

of the triple-frequency phase wind-up amounts to only 1.2 mm for the given frequencies. As such, phase-windup effects are typically masked by receiver noise and might also be neglected in the present application.

Transmit antenna phase patterns for use in the triple-frequency combination are not known beforehand, but can be constructed in a residuals stacking approach (Jäggi et al., 2009). Representative amplitudes of the triple-frequency phase patterns obtained in this way for the various GLONASS satellites are at the level of a few millimeters.

Daily estimates of $\boldsymbol{d}_{\mathrm{tri}}$ for the well observed M+ and K1B satellites exhibit seasonal variations with an overall 1-σ scatter of about 1 cm, 0.3 cm, and 3 cm in the x-, y-, and z-components. A similar dispersion applies for the satellite-specific mean values within each block (Fig. 4). As an exception, notably larger uncertainties apply for the latest K1B satellite R807 which is affected by non-orbit-related inter-frequency biases of varying periodicity that strongly contaminate the triple-carrier baseline analysis (Steigenberger and Montenbruck, 2024).

In the case of the new GLONASS-K2 satellite, consideration of the harmonic bias model (9) shows dominant contributions at once and twice the orbital period. With representative values of 1–10 mm, the individual harmonics are notably smaller than encountered on the GPS IIF satellites (Montenbruck et al., 2012), but show a similar decrease of their amplitude with increasing Sun elevation β above the orbit plane. On the other hand, the x-component of the antenna baseline shows an increased correlation with harmonic bias variations at larger

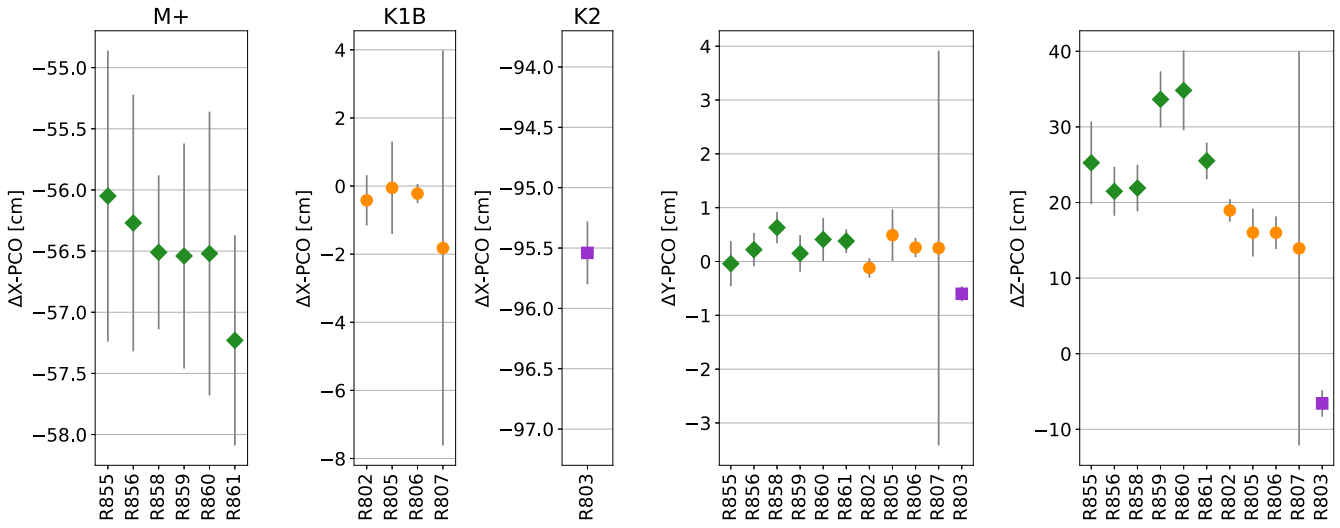

Fig. 4. Estimated values of the triple-frequency antenna offset combination $\boldsymbol{d}_{\mathrm{tri}}$ for GLONASS-M+, -K1, and -K2 satellites. Gray bars mark the 1-σ dispersion of daily estimates.

β-angles, thus causing pronounced, β-dependent errors when neglecting such biases in the K2 baseline estimation. Compared to Dilssner and Springer (2024), who use a simplified observation model without temporal bias variations, the joint estimation of harmonic bias parameters along with the antenna baseline reduces the scatter of the estimated x-component of K2 from about 5 cm to a level of about 1 cm. This order of mangitude is similar to that of other M+ and K1 satellites and avoids a dependence of the long-term average on the duration of the overall data arc. Consideration of the harmonic biases is likewise important for a trustworthy attitude determination from triple-frequency observations as will be discussed in Section 4.4.

Block-mean values of the triple-frequency baseline estimates are summarized in Table 2 and compared with manufacturer PCOs and data from the navigation messages. As shown in Eq. (8), the estimated values actually describe a linear combination of the difference between L3 CDMA and L2 FDMA PCOs and the difference between L2 and L1 FDMA PCOs. Given the rotationally symmetric antenna design, it is reasonable to assume identical locations of all phase centers on their boresight axis independent of the specific signal frequency and thus identical horizontal (x/y) components of the L1 and L2 FDMA phase centers. The x-/y-offsets of the L3 CDMA phase center from the L1/L2 FDMA phase center obtained in this way agree to about 1 cm with the manufacturer values and phase center offsets derived from the FDMA − CDMA ephemeris difference. In the case of the K2 satellite, the relative position of the FDMA and CDMA antennas in the x/y-plane as obtained from the triple-frequency carrier phase observations is, furthermore, consistent with the design drawing shown in Steigenberger (2023) to 0.5 cm.

The z-components of the estimated triple-frequency PCO combination show good (3 cm) consistency with manufacturer and provider data for GLONASS-M+ satellites when considering L3OC PCOs from the L3OC navigation message, but agree less favorably (+15 cm) when using L3OC PCOs from Fatkulin (2015). For GLONASS-K1B satellites and the new K2 satellite, mean differences of +14 cm and −8 cm are obtained (Table 2).

3.3. GLONASS reference PCOs

Based on the individual data discussed above, a synthesized set of reference PCOs has been compiled for the various blocks of modernized GLONASS satellites, which is shown in Table 3. Manufacturer and provider data are adopted for the horizontal antenna positions as well as the L1 and L2 z-PCOs of the FDMA and CDMA antennas, while the z-component of the L3 CDMA antenna is derived from triple-frequency baseline estimates along with the adopted L1/L2 PCOs.

For further reference, Table 3 also provides the corresponding PCO values for the ionosphere-free linear combination of L1 and L2 FDMA observations for frequency channel $k = 0$. These may be used along with observed L1/L2 FDMA PCOs in the current igs20.atx antenna model (Rebischung et al., 2022) to compute satellite-specific L1/L2 PCO differences with respect to the block-mean manufacturer values. Upon adding these differences to the individual reference PCOs in Table 3, a refined antenna model with satellite- and frequency-specific GLONASS PCO values can then be obtained, which is consistent with L1, L2, and L3 carrier phase observations and aligned to the IGS20 reference frame. Use of such a model would retain compatibility with current processing con-

Table 3
Antenna- and frequency-specific reference PCOs for modernized GLONASS satellites. All values in [m]. Subscripts C and F denote CDMA and FDMA values, respectively.

Satellite type	Band	PCO
GLONASS M+	$L1_F$	$(-0.545, 0.000, +2.099)$
	$L2_F$	$(-0.545, 0.000, +1.969)$
	$L3_C$	$(-1.100, 0.000, +2.215)$
	$IF(L1_F/L2_F)$	$(-0.545, 0.000, +2.298)$
GLONASS K1B	$L1_F$	$(0.000, 0.000, +1.561)$
	$L2_F$	$(0.000, 0.000, +1.431)$
	$L3_C$	$(0.000, 0.000, +1.568)$
	$IF(L1_F/L2_F)$	$(0.000, 0.000, +1.760)$
GLONASS K2	$L1_F$	$(+0.960, 0.000, +0.975)$
	$L2_F$	$(+0.960, 0.000, +0.844)$
	$L1_C$	$(0.000, 0.000, +0.975)$
	$L2_C$	$(0.000, 0.000, +0.844)$
	$L3_C$	$(0.000, 0.000, +0.752)$
	$IF(L1_F/L2_F)$	$(0.000, 0.000, +1.176)$

cepts based on a ionosphere-free L1/L2 dual-frequency combination but pave the way for a transition to L1/L3 dual-frequency processing or an uncombined processing of all available GLONASS signals (Strasser et al., 2019).

4. Attitude

GNSS satellites in medium Earth orbit apply a continuous yaw steering to orient the solar panel axis perpendicular to the Sun and Earth directions. For a nadir pointing z-axis, the orientation of the spacecraft body frame relative to the Earth-pointing frame is described by right-handed rotation about the nadir-pointing z-axis by the yaw angle ψ. This is schematically shown in Fig. 5 for the example of the GLONASS-K2 platform. In nominal yaw-steering mode, the yaw angle attains the value

$$\psi = \mathrm{atan2}(-\tan\beta, \sin\mu) \tag{11}$$

(Bar-Sever, 1996; Kouba, 2009; Montenbruck et al., 2015) where β denotes the Sun elevation above the orbital plane and μ is the satellite's orbit angle relative to the midnight line.

During phases of low β-angles, the GLONASS satellites apply a rate-limited yaw steering, whenever the nominal yaw rate during noon and midnight turns would exceed a design-specific limit. However, different concepts apply for the specific yaw angle profile adopted by the various satellite generations.

4.1. GLONASS-M/M+ rate-limited yaw steering

For GLONASS-M and -M+ satellites, the detailed yaw steering law has not been disclosed, but an empirical model has been established by Dilssner et al. (2011) from the analysis of yaw angle measurements obtained with a reverse kinematic precise point positioning (RKPPP) technique. Based on this, a maximum yaw rate of

$$\omega_{\mathrm{max,GLO-M/M+}} \approx 0.24 - 0.26^\circ/\mathrm{s} \tag{12}$$

has been determined. For noon turns, the yaw slew is performed symmetrically around the noon line, i.e., the epoch at which the orbit angle μ amounts to 180°, and the duration is chosen such as to match the nominal yaw angles at the start and end of the constant-rate yaw rotation. In midnight turns, a maximum-rate slew is initiated upon entering the eclipse zone. The slew continues until the yaw angle attains a value matching the nominal yaw angle at the eclipse exit. The yaw angle is then held fixed until the satellite actually leaves the eclipse. Thereafter, a nominal yaw-steering attitude profile is resumed.

An obvious simplification of the Dilssner et al. (2011) model relates to the fact that it neglects the time needed for accelerating and decelerating the spacecraft at the begin and end of the maximum-rate slew. A rigorous modeling of these phases would require knowledge of the corresponding torques and moments of inertia, which is not presently available for GLONASS-M/M+ satellites and cannot be retrieved from observations with adequate precision. From a practical point of view, the instantaneous transition between a nominal yaw steering and a maximum rate slew appears of limited impact and the model is successfully applied for GLONASS-M/M+ precise orbit determination and precise point positioning by IGS analysis centers with a reference value of $\omega_{\mathrm{max,GLO-M/M+}} = 0.25\,^\circ/\mathrm{s}$.

4.2. GLONASS-K rate-limited yaw steering

As discussed in the previous section, the GLONASS-K1B satellites exhibit a close-to-zero offset of the L-band antenna from the yaw axis. Therefore, the RKPPP method can at best provide a coarse yaw angle estimation and no effort has been made so far to establish an empirical GLONASS-K1 attitude model for low β-angles. However, the basic properties of the yaw steering for these satellites have first been disclosed in Fateev et al. (2013, 2014) and were later specified for GLONASS users as part of the GLONASS CDMA signal ICD (Russian Space Systems, 2016d). Relevant parameters for modeling the yaw slew in the user receiver are provided as part of the CDMA attitude message (see Section 2), which is transmitted in the vicinity of a rate-limited yaw slew.

Based on the ICD specification, the GLONASS-K1/K2 satellites apply a rate-limited yaw steering, whenever the nominal yaw rate during noon and midnight turns exceeds a limit ω_{max}. Consistent with early assumptions in Fateev et al. (2013), the CDMA attitude messages report a common value of

$$\omega_{\mathrm{max}} = 0.249\ 87^\circ/\mathrm{s}. \tag{13}$$

for the peak rotation rate of all GLONASS-K1B and -K2 satellites, despite obvious differences in the platform design and the corresponding moments of inertia about the yaw axis. This value is also in good agreement with the maximum angular velocity of GLONASS-M/M+ yaw slews observed by Dilssner et al. (2011).

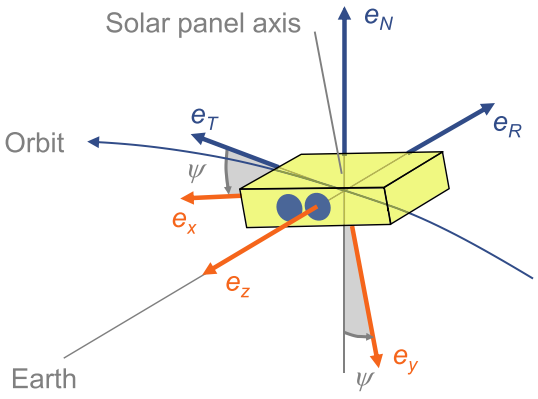

Fig. 5. Illustration of the yaw angle ψ describing the orientation of the GLONASS-K2 spacecraft body-frame $(\mathbf{e}_x, \mathbf{e}_y, \mathbf{e}_z)$ relative to the orbital frame with unit vectors in radial, along-track and orbit-normal direction $(\mathbf{e}_R, \mathbf{e}_T, \mathbf{e}_N)$ following IGS axis conventions.

For orbit angles near $\mu = 0$ (midnight) and $\mu = \pi$ (noon) and small β-angles, Eq. (11) for the nominal yaw angle can be approximated by

$$\cot\psi = -\frac{\mu}{\beta}. \tag{14}$$

This yields a nominal yaw rate of

$$\omega = |\dot{\psi}| \approx \sin^2\psi \cdot \frac{\dot{\mu}}{|\beta|}, \tag{15}$$

which attains a peak value of $\dot{\mu}/|\beta|$ at the noon or midnight point ($\psi = \pm\pi/2$). Like for the GLONASS-M/M+ satellites, rate-limited yaw slews of K1B and K2 satellites are thus required for

$$|\beta| < \frac{\dot{\mu}}{\omega_{\max}} \approx 2.0^\circ, \tag{16}$$

where

$$\dot{\mu} \approx 0.155 \text{ mrad/s} = 0.008\,88^\circ/\text{s} \tag{17}$$

is the orbital angular rate of the GLONASS satellites at an orbital altitude of 19 130 km. At the given slew rates, a yaw maneuver can typically be completed in less than 15 min, during which the variation of the β-angle can essentially be neglected.

Other than for GLONASS-M/M+ satellites, which start their midnight turns at the eclipse entry (Dilssner et al., 2011), the rate-limited yaw maneuvers of both noon and midnight turns are performed symmetrically with respect to the noon or midnight point in the case of K1 and K2 satellites. The attitude slew is introduced by a ramp-up phase of duration τ_a, during which the yaw rate is linearly increased from its value ω_{in} at the maneuver start to the intended maximum rate $\omega_{\max}$. This is followed by a phase of duration $2\tau_b$ with constant yaw rate $\omega_{\max}$, and a ramp-down phase of duration τ_a, during which the yaw rate is again decreased from $\omega_{\max}$ to $\omega_{\text{out}} = \omega_{\text{in}}$ (Fig. 6).

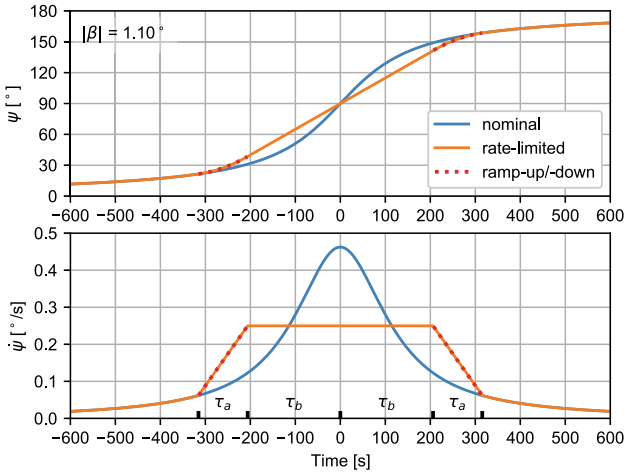

Fig. 6. Illustration of GLONASS-K yaw angle and rate profile during rate-limited yaw slews. Time is measured relative to the spacecraft noon or midnight epoch.

Based on the parameters transmitted in the CDMA attitude messages, the rate change is performed with a common value

$$\dot{\omega} = 0.03 \text{ mrad/s}^2 = 1.7188 \times 10^{-3}\,^\circ/\text{s}^2 \tag{18}$$

of the angular acceleration for the K1B and K2 satellites. The duration of the ramp-up phase as well as the final ramp-down phase can be computed from

$$\tau_a = \frac{\omega_{\max} - \omega_{\text{in}}}{\dot{\omega}}, \tag{19}$$

which results in a maximum value of about 145 s. The actual duration is typically shorter, since the yaw maneuver always starts and ends at a non-zero yaw rate $\omega_{\text{in}} = \omega_{\text{out}}$ that reflects the rate of nominal yaw steering at the respective epochs.

The accumulated yaw-angle change at the mid maneuver epoch $\tau_{\text{mid}} = \tau_{\text{in}} + \tau_a + \tau_b$ amounts to

$$\begin{aligned} \Delta\psi &= |\psi_{\text{mid}} - \psi_{\text{in}}| = \tfrac{1}{2}|\psi_{\text{out}} - \psi_{\text{in}}| \\ &= \omega_{\text{in}} \cdot \tau_a + \tfrac{1}{2}\dot{\omega} \cdot \tau_a^2 + \omega_{\max} \cdot \tau_b \\ &= \tfrac{1}{2}(\omega_{\text{in}} + \omega_{\max}) \cdot \tau_a + \omega_{\max} \cdot \tau_b \end{aligned} \tag{20}$$

and matches

$$\Delta\psi = \left|\psi_{\text{in}} + \text{sign}(\beta) \cdot \frac{\pi}{2}\right| = \left|\psi_{\text{out}} + \text{sign}(\beta) \cdot \frac{\pi}{2}\right| \tag{21}$$

with $-\pi < \psi_{\text{in}}, \psi_{\text{out}} < +\pi$ if the maneuver is centered around the noon-midnight line.

Assuming small values $\sin\mu \approx \mu$ near the noon-midnight line and a constant orbital angular rate $\dot{\mu}$, the yaw angle variation $\Delta\psi$ between maneuver start and center can be approximated by

$$\tan\Delta\psi = \frac{\dot{\mu}}{|\beta|}\tau. \tag{22}$$

Neglecting the ramp-up phase, i.e., assuming an infinite value of $\dot{\omega}$, the semi-duration $\tau = \tau_b$ of a rate-limited yaw maneuver for a given β-angle is thus described by the relation

$$|\beta| \tan(\omega_{\max}\tau) = \dot{\mu}\tau. \tag{23}$$

In the absence of a closed-form solution, a Newton–Raphson iteration

$$\tau_{i+1} = \tau_i - y(\tau_i)/y'(\tau_i) \tag{24}$$

can be applied to find to find the root of

$$y(\tau) = |\beta| \tan(\omega_{\max}\tau) - \dot{\mu}\tau \tag{25}$$

with the derivative

$$y'(\tau) = \frac{|\beta|\omega_{\max}}{\cos^2(\omega_{\max}\tau)} - \dot{\mu}. \tag{26}$$

A suitable starting value is given by the arithmetic mean

$$\tau_0 = \frac{\pi/2 + \arccos(|\beta|\omega_{\max}/\dot{\mu})}{2\omega_{\max}} \tag{27}$$

of the duration of a 90° slew and the local extreme value of y (i.e., the root of y'). This enables convergence to better than 1 s within less than about 10 iterations over the applicable range of β-angles (i.e., $|\beta| < \dot{\mu}/\omega_{\max}$).

Given the initial guess τ of the maneuver-semi-duration obtained from the maximum-rate yaw maneuver approximation, a fixed-point iteration can be applied to obtain refined estimates of the maneuver parameter including the ramp-up phase. For a given value of τ, the yaw-angle difference $\Delta\psi$ relative to the mid maneuver epoch and the nominal yaw rate ω_{in} are obtained as

$$\Delta\psi = \arctan\left(\frac{\dot{\mu}}{|\beta|}\tau\right) \tag{28}$$

and

$$\omega_{\text{in}} = \frac{1}{1+\tan^2\Delta\psi} \cdot \frac{\dot{\mu}}{|\beta|} = \frac{\dot{\mu}|\beta|}{(\dot{\mu}\tau)^2 + \beta^2}. \tag{29}$$

Based on these, the ramp-up duration τ_a and the semi-duration τ_b of the constant-rate yaw rotation can be computed from Eq. (19) as well as

$$\tau_b = \frac{1}{\omega_{\max}}\left(\Delta\psi - \frac{1}{2}(\omega_{\text{in}} + \omega_{\max}) \cdot \tau_a\right). \tag{30}$$

This yields a refined estimate $\tau = \tau_a + \tau_b$ of the maneuver semi-duration based on which the iteration can be continued. Again, less then 10 steps are typically required to obtain τ_a and τ_b with a 1-s precision.

While real-time navigation users can generally use the information from the CDMA attitude message, the algorithms presented above enable an independent computation of the yaw profile for rate-limited attitude maneuvers in the low β-angle regime based on the known Sun-spacecraft-Earth geometry. This is of primary interest for GLONASS-K precise orbit determination and precise point positioning applications that require concise attitude data for modeling the antenna phase center location (Loyer et al., 2021).

Results of the GLONASS-K attitude maneuver model for a representative set of β-angles are summarized in Table 4. As may be seen, the ramp-up phase τ_a constitutes a notable fraction of the overall yaw slew and attains a peak value of roughly one-third of the total duration $\tau_a + \tau_b$ from the slew start to the maneuver center at low β-angles. The maximum total maneuver duration is attained near $\beta = 0°$ and amounts to roughly 720 s for the peak rate and acceleration specified in the CDMA navigation messages.

For comparison, Table 4 also provides the parameters of a simplified rate-limited yaw model, which neglects the ramp-up phase. This model is equivalent to the GLONASS-M/M+ noon turn model of Dilssner et al. (2011) and corresponds to an infinite angular acceleration $\dot{\omega} = \infty$ in the full model. As may be recognized, the actual slew maneuver starts up to roughly one minute earlier than described by the simplified model. Depending on the β-angle, the yaw angles predicted by the full and simplified model may exhibit peak differences of about 4°. At a horizontal antenna offset of 1 m, a yaw error of this magnitude would result in a 7 cm difference of the modeled antenna phase center position and a peak range error of about 2 cm. While this exceeds the targeted modeling accuracy in precise point positioning applications, the simplified model is computationally less demanding and therefore lends itself as a viable alternative for practical applications. As an alternative, Table 4 may be used as a look-up table for the individual maneuver parameters in real-time data processing with limited computational resources.

4.3. CDMA attitude message parameters

As part of the GLONASS CDMA attitude message, all parameters required for computing the yaw angle during rate-limited yaw steering maneuvers are transmitted to the user in the vicinity of such maneuvers. Aside from

Table 4
Parameters of GLONASS-K rate-limited yaw slews as a function of the β-angle. For comparison, the initial yaw angle $\psi_{\text{in},0}$ and the semi-duration τ_0 for a simplified (infinite acceleration) model without ramp-up phase as well as the peak yaw angle difference $\max|\delta\psi_{\text{in}}|$ and the semi-duration difference $\delta\tau$ between the full and simplified model are given.

$\lvert\beta\rvert$ [°]	ψ_{in} [°]	τ_a [s]	τ_b [s]	$\psi_{\text{in},0}$ [°]	τ_0 [s]	$\max\lvert\delta\psi_{\text{in}}\rvert$ [°]	$\delta\tau$ [s]
0.20	3.1	141	275	3.7	345	4.1	71
0.40	6.5	136	262	7.8	329	3.9	69
0.60	10.2	130	248	12.3	311	3.4	67
0.80	14.2	123	232	17.2	291	3.0	64
1.00	18.9	114	215	22.7	269	2.5	60
1.20	24.3	104	196	28.9	244	2.0	56
1.40	30.9	90	175	36.2	215	1.4	50
1.60	39.7	70	148	45.0	180	0.9	38
1.80	53.0	40	113	56.6	134	0.4	19
2.00	76.8	5	48	76.8	53	0.0	0

the fixed values of the maximum yaw rate $\omega_{\max}$ and the angular acceleration $\dot{\omega}$ already mentioned above, the message provides the yaw angle ψ_{in}, the magnitude ω_{in} of its derivative at the maneuver start, as well as a sign flag indicating the direction of the slew maneuver. In addition, the slew start time t_{in} as well as the time offsets $\tau_1 = \tau_a$ and $\tau_2 = \tau_a + 2\tau_b$ describing the begin and end of the maximum rate phase relative to the maneuver start are given. For completeness, we note that yaw angles in the GLONASS attitude message are mapped to a range of $[0, 2\pi[$ and sign-inverted with respect to the present convention (see Fig. 5) due to a different choice of reference axes.

Even though the CDMA attitude model would at least be applicable for noon turns of the GLONASS-M/M+ satellites, the corresponding attitude message is presently only transmitted by GLONASS-K2 and -K1B satellites. Using two JAVAD TRE-3S receivers located in Oberpfaffenhofen, Germany, and Sydney, Australia, that are equipped with an ICD-2016-compatible prototype firmware, raw CDMA navigation data frames with attitude messages for 26 noon/midnight turns of three satellites (R805, R803, and R806) could be recorded during the eclipse seasons of GLONASS planes 2, 1, and 3 in early November 2023, mid January 2024, and late February 2024.

Comparison of the transmitted and modeled maneuver parameters shows a proper consistency in most cases. Median differences of the maneuver start times and the ramp-up/-down durations amount to 2 s and 0.5 s with peak differences of about 8 s and 4 s, respectively. The yaw angles at the maneuver start agree at a level of 0.2° with a peak error of 1.6°, while the angular rates at the maneuver start indicate consistency of the β-angles used in the maneuver modeling of better than 0.01°. As an exception, major discrepancies were found in the transmitted values of τ_2. These differed from the expectation by an error varying almost linearly between a peak value 140 s for near-zero β-angles and near-zero at $\beta \approx 2°$. It is presently unclear, whether the differences relate to actual errors in the generation of maneuver parameters and navigation messages within the GLONASS control segment and satellites or a misinterpretation of the τ_2 parameter field in the decoding of raw navigation data frames within the present study. Further data sets and independent analyses will likely be required to trace down the root cause of this discrepancy. As a substitute, the value can be recomputed from trustable attitude maneuver parameters using Eq. (30) along with the relation $\tau_2 = \tau_1 + 2\tau_b$.

4.4. Yaw-angle estimation

As suggested in Hauschild (2019), triple-carrier measurements from multiple antennas can be used to measure the yaw-angle profile of a GNSS satellite. Compared to the RKPPP technique, the approach avoids the need for a precise modeling of individual pseudorange and carrier phase observations, since geometric range contributions, such as the satellite-to-station distance, clock offsets, and atmospheric delays, are readily eliminated by the triple-carrier combination.

The attitude determination makes use of the same observation model as the triple-frequency baseline estimation (Eq. 7), but now assumes the vector $\boldsymbol{d}_{\text{tri}}$ as a known quantity, while treating the spacecraft yaw angle ψ as an unknown. The observed triple-frequency carrier phase combination can be related to the unknown yaw angle, the carrier phase ambiguities, and, optionally, harmonic bias coefficients. In view of the nonlinear dependence of $\boldsymbol{R}_z$ on the yaw angle, an iterated least-squares estimation is required to determine the individual parameters from the observed values of φ_{tri}. For this purpose, the transformation matrix

$$\boldsymbol{R}_z(t) = \boldsymbol{R}_z(\psi_{\text{ref}}(t)) + \left.\frac{d\boldsymbol{R}_z(\alpha)}{d\alpha}\right|_{\psi_{\text{ref}}(t)} \cdot \Delta\psi(t), \tag{31}$$

is linearized about a reference yaw angle $\psi_{\text{ref}}(t)$ with $\Delta\psi(t) = \psi(t) - \psi_{\text{ref}}(t)$. The estimation vector then includes the vector of epoch-wise yaw angle corrections $\Delta\psi(t)$, the vector of ambiguities A_{tri} for all continuous tracking arcs of the observing stations, and the bias parameters $(b_{c,1}, b_{s,1}, \ldots, b_{c,3}, b_{s,3})$. Starting from, e.g., the nominal yaw steering, improved estimates of the true yaw angle as well as the other estimation parameters can thus be estimated in an iterative manner.

Using a global network of 100–150 stations supporting L1/L2 FDMA and L3 CDMA tracking, yaw angle estimates of the GLONASS M+ satellites exhibit a representative noise level of 0.7–0.8°. By way of example, differences between estimated and nominal yaw angles are illustrated in Fig. 7 for a one-day sample data arc of R860 data collected at an intermediate β-angle. These differences include the joint contributions of attitude estimation and control errors and provide an upper limit for the actual attitude stability. For the K2 satellite, 1-σ differences of about 0.6° are obtained during the nominal yaw steering phase, which complies with earlier descriptions of attitude and orbit control (AOCS) system improvements in the recent generations of GLONASS satellites (Revnivykh et al., 2017). Compared to Dilssner and Springer (2024), a notably improved consistency of K2 attitude estimates with the nominal yaw profile is obtained in the present study as a result of considering periodic phase bias variations in the processing of the triple-frequency carrier phase observations.

Examples of yaw angle estimates in the vicinity of noon and midnight turns are shown in Fig. 8 for a sample GLONASS-M+ satellite and the first GLONASS-K2 satellite. While day-time turns are performed symmetrically around the noon epoch for both types of spacecraft, a different approach is used for the night-time slews. These are initiated at the eclipse entrance on GLONASS-M+ satellites, but are placed symmetrically to the noon-midnight line on the K2 satellite. However, a similar rotation rate

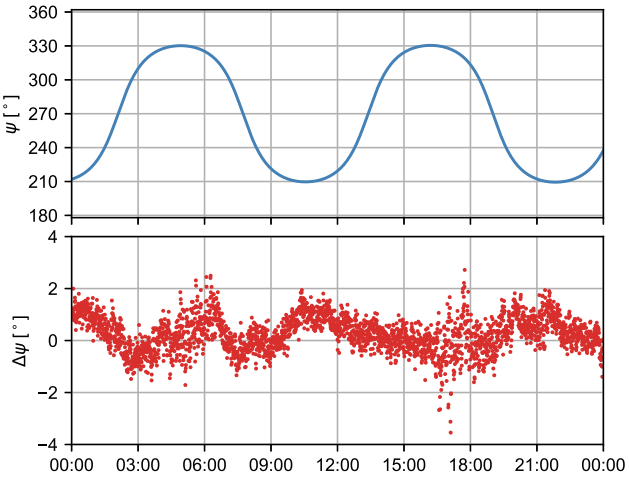

Fig. 7. Example of GLONASS-M+ attitude stability for R860 on January 11, 2024 ($\beta = 29.6°$). Nominal yaw angles are illustrated in the upper graph, differences of estimated and nominal yaw angles are shown in the bottom plot.

of about 0.25°/s applies in all cases despite the widely different platform design of the two types of spacecraft.

With the exception of a $\pm 180°$ yaw slew at $\beta \approx 0°$ that was performed near 09:30 on Jan 12, 2024 in a different direction than expected from the offline computation, the K2 satellite showed differences at the 1–4° level relative to the reference model for rate-limited yaw maneuvers during the first period of $|\beta| < 2°$ in mid January 2024. Slightly larger errors were encountered during M+ midnight turns, which can largely be attributed to a different modeling of the eclipse start time in the AOCS. On the other hand, substantial deviations of up to 20° from the widely adopted empirical model of Dilssner et al. (2011) could be noted over a period of a few hundred seconds in the rate limited noon slews of the M+ satellites. While a constant rate is assumed in this model based on earlier RKPPP analyses of GLONASS-M satellites, the M+ yaw profiles derived from triple-frequency observations provide clear evidence of a yaw acceleration during the final phase of the yaw maneuver. As illustrated in Fig. 9 for a representative example of the R859 satellite, the anomalous acceleration starts in the second half of the maneuver and results in a 0.10–0.15 °/s excess yaw rate relative to the assumed value of $\dot{\psi} = 0.25$ °/s. The rationale for this feature, which had not been noted in earlier analyses of GLONASS-M satellites, remains unknown, but suggests a need for further monitoring to best support precise orbit determination and PPP with GLONASS-M and -M+ satellites during the eclipse season.

5. Summary and conclusions

Within this study, we present a comprehensive analysis of GLONASS CDMA and FDMA observations and navigation messages for characterizing the band-specific phase center locations of CDMA and FDMA antennas as well as the yaw steering profiles of GLONASS-M+, -K1B, and -K2 satellites. PCO values from previously released manufacturer data, parameters of the L3OC and L1OC navigation message, and differences of satellite positions computed from CDMA and FDMA ephemerides are presented and compared with the results of a triple-frequency carrier phase analysis. The results are used to establish a set of block-specific reference PCOs for each frequency band and respective antennas. Upon alignment with the L1/L2 PCOs of the current IGS antenna model, a refined model offering a complete set of frequency-wise and antenna-specific PCOs of each individual GLONASS

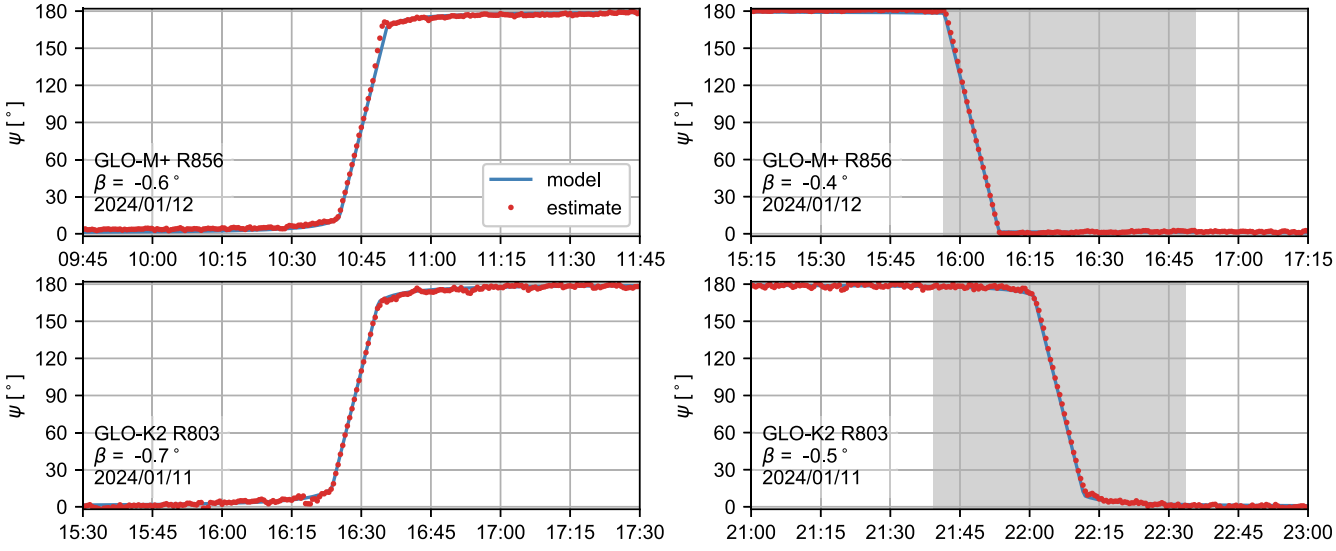

Fig. 8. Comparison of estimated and modeled yaw-angle profiles during noon (left) and midnight turns (right) at low β angles for a GLONASS-M+ (top) satellite and the new GLONASS-K2 satellite (bottom). Eclipse periods are marked by a shaded background.

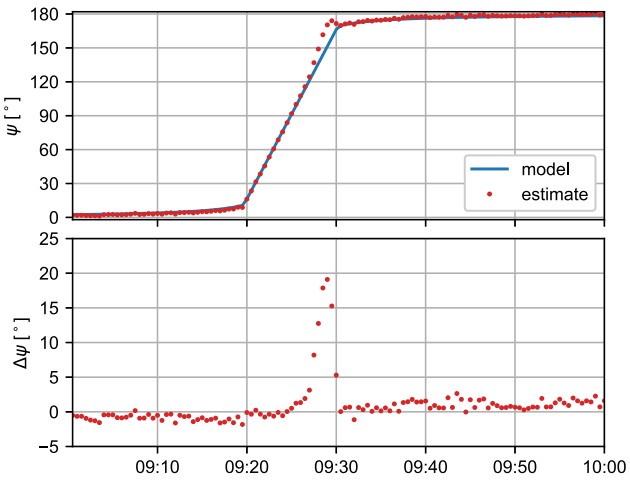

Fig. 9. Systematic yaw offsets during noon turns of the GLONASS-M+ satellite R859 on January 12, 2024 ($\beta = -0.5°$): nominal and estimated yaw angle (top), difference (bottom). Individual samples of the estimated yaw angle are separated by 30 s.

satellite can be established that will assist a future transition from ionosphere-free dual-frequency processing of GLONASS observations to an uncombined, multi-frequency processing approach.

Similar to other GNSS satellites in medium Earth orbit, GLONASS satellites replace the nominal yaw steering that enables an Earth pointing antenna and a Sun-pointing solar panel orientation by a rate-limited yaw steering during periods of low Sun elevation above the orbital plane. Other than the GLONASS-M/M+ satellites, the K1B and K2 satellites align the center-time of all attitude slews in the low β-angle regime with the respective noon or midnight epoch. A generic description of the respective yaw profile involving a ramp-up phase with constant yaw acceleration, a phase with constant yaw rate, and a final ramp-down phase is provided in the CDMA interface control document. Relevant maneuver parameters are transmitted in the CDMA navigation messages of K1B and K2 satellites for proper modeling of the phase center in real-time navigation applications. As part of this study, an iterative algorithm enabling an independent computation of the maneuver start time and the duration of the accelerated and constant-rate maneuver phase is presented that extends the availability of attitude model parameters to precise point positioning users and GLONASS orbit determination.

Based on the use of distinct antennas for the transmission of L3 CDMA and L1/L2 FDMA signals on the GLONASS-M+ satellites and the recently launched K2 satellite, the instantaneous yaw angle of these satellites can be estimated using a triple-frequency combination of the respective carrier phase observations. The measured yaw angles confirm a good consistency of the actual yaw profile during noon and midnight turns with the corresponding models, as well as the use of a common design value $\omega_{max} = 0.25°/s$ of the maximum yaw rate for a widely different set of spacecraft platforms. For the K2 satellite, consistency at the 1° level between the modeled yaw angles and the estimated values is obtained, when accounting for the presence of orbit periodic biases between FDMA and CDMA signals. For GLONASS M+ satellites, anomalous yaw accelerations during rate-limited noon turns could be revealed that cause yaw offsets of up to 20° with respect to established GLONASS-M attitude models. Overall, the triple-carrier technique lends itself as a viable tool for continued monitoring of GLONASS-M+ and -K2 yaw angles. This may provide a useful alternative to purely model-based attitude profiles in post-processed GLONASS products.

Data availability

L1 and L2 FDMA as well as L3 CDMA observations of GLONASS satellites from a world-wide network of multi-GNSS monitoring stations and cumulative broadcast ephemerides are freely provided by the global data centers of International GNSS Service, including CDDIS (Noll, 2010, https://cddis.nasa.gov/archive/gnss/data/) and IGN (https://igs.ign.fr/pub/igs). GNSS observation data of the Plate Boundary Observatory and SuomiNet are available at the Geodetic Facility for the Advancement of Geoscience (GAGE, https://www.unavco.org/what-we-do/gage-facility/). L1OC/L3OC navigation data collected by the authors can be made available on reasonable request.

Declaration of Competing Interest

The authors declare that they have no known competing financial interests or personal relationships that could have appeared to influence the work reported in this paper.

Acknowledgments

The authors are grateful to Peter Mumford and Craig Roberts for their continued effort in operating the UNSW GNSS monitoring station. JAVAD GNSS Europe is acknowledged for the provision of a prototype firmware supporting L1OC, L2OC, and L3OC tracking as well as extraction of raw navigation data frames. Furthermore, we acknowledge the continued effort of the IGS and its data centers to collect, process, and share GNSS data and products of the highest precision and reliability.

References

Bar-Sever, Y.E., 1996. A new model for GPS yaw attitude. J. Geod. 70 (11), 714–723. https://doi.org/10.1007/BF00867149.

Daly, P., Riley, S., 1994. GLONASS P-code data message. In ION NTM 1994, pp. 195–202.

Deshpande, S., Kumar, S., Shekar, Y., 2011. Efficient numerical integration method of GLONASS satellite position computation. In: ION GNSS 2011, pp. 775–779.

Dilssner, F., Springer, T., 2024. GLONASS-K attitude: rapid turning maneuvers and other deviations from ideal yaw steering. GPS Solut. 28 (3), 144. https://doi.org/10.1007/s10291-024-01691-x.

Dilssner, F., Springer, T., Gienger, G., et al., 2011. The GLONASS-M satellite yaw-attitude model. Adv. Space Res. 47 (1), 160–171. https://doi.org/10.1016/j.asr.2010.09.007.

Fateev, A.V., Emelyanov, D.V., Tentilov, U.A., et al., 2014. Passage of special orbital sections by a navigation spacecraft of the GLONASS system. Siberian Aerospace J. 15 (4), 126–131 (in Russian).

Fateev, A.V., Emelyanov, D.V., Tentilov, U.A., et al., 2013. Algorithms for determining the heading angle for calculating the phase center of the GLONASS spacecraft during preemptive rollout sections. Siberian Aerospace J. 14 (4), 198–202 (in Russian).

Fatkulin, R., 2015. GLONASS satellite geometry and attitude models, eMail to O. Montenbruck, 2015/04/20.

Gini, F., 2023. RINEX, The Receiver Independent Exchange Format, Version 4.01. Technical Report IGS/RTCM. URL: https://files.igs.org/pub/data/format/rinex_4.01.pdf.

Hauschild, A. (2017). Basic observation equations. In: Teunissen, P., Montenbruck, O. (Eds.), Springer Handbook of Global Navigation Satellite Systems chapter 19, pp. 561–582. https://doi.org/10.1007/978-3-319-42928-1_19.

Hauschild, A., 2019. GNSS yaw attitude estimation: Results for the Japanese Quasi-Zenith Satellite System Block-II satellites using single- or triple-frequency signals from two antennas. Navigation 66 (4), 719–728. https://doi.org/10.1002/navi.333.

Ilcev, D.S., 2007. Cospas-Sarsat LEO and GEO: Satellite distress and safety systems (SDSS). Int. J. Satell. Comm. N. 25 (6), 559–573. https://doi.org/10.1002/sat.881.

Jäggi, A., Dach, R., Montenbruck, O., et al., 2009. Phase center modeling for LEO GPS receiver antennas and its impact on precise orbit determination. J. Geod. 83 (12), 1145–1162. https://doi.org/10.1007/s00190-009-0333-2.

Johnston, G., Riddell, A., Hausler, G., 2017. The International GNSS Service. In: Teunissen, P., Montenbruck, O. (Eds.), Springer Handbook of Global Navigation Satellite Systems chapter 33. Springer, pp. 967–982. https://doi.org/10.1007/978-3-319-42928-1_33.

Kouba, J., 2009. A simplified yaw-attitude model for eclipsing GPS satellites. GPS Solut. 13 (1), 1–12. https://doi.org/10.1007/s10291-008-0092-1.

Loyer, S., Banville, S., Geng, J., et al., 2021. Exchanging satellite attitude quaternions for improved GNSS data processing consistency. Adv. Space Res. 68 (6), 2441–2452. https://doi.org/10.1016/j.asr.2021.04.049.

Montenbruck, O., Hugentobler, U., Dach, R., et al., 2012. Apparent clock variations of the Block IIF-1 (SVN62) GPS satellite. GPS Solut. 16 (3), 303–313. https://doi.org/10.1007/s10291-011-0232-x.

Montenbruck, O., Schmid, R., Mercier, F., et al., 2015. GNSS satellite geometry and attitude models. Adv. Space Res. 56 (6), 1015–1029. https://doi.org/10.1016/j.asr.2015.06.019.

Montenbruck, O., Steigenberger, P., 2022. BRD400DLR: DLR's merged multi-GNSS broadcast ephemeris product in RINEX 4.00 format. https://doi.org/10.57677/BRD400DLR.

Noll, C.E., 2010. The Crustal Dynamics Data Information System: A resource to support scientific analysis using space geodesy. Adv. Space Res. 45 (12), 1421–1440. https://doi.org/10.1016/j.asr.2010.01.018.

Povalyaev, A., 2013. GLONASS navigation message format for flexible row structure. In: ION GNSS+ 2013, pp. 972–974.

Rebischung, P., Altamimi, Z., Métivier, L., et al., 2024. Analysis of the IGS contribution to ITRF2020. J. Geod. 98 (6), 49. https://doi.org/10.1007/s00190-024-01870-1.

Rebischung, P., Villiger, A., Masoumi, S. et al., 2022. [IGSMAIL-8238] Upcoming switch to IGS20/igs20.atx and repro3 standards, URL: https://lists.igs.org/pipermail/igsmail/2022/008234.html.

Revnivykh, S., Bolkunov, A., Serdyukov, A., et al., 2017. GLONASS. In: Teunissen, P., Montenbruck, O. (Eds.), Springer Handbook of Global Navigation Satellite Systems chapter 8, pp. 219–245. https://doi.org/10.1007/978-3-319-42928-1_8.

RISDE (2008). GLONASS Interface Control Document: Navigation radiosignals in bands L1, L2 (Version 5.1). Technical Report Russian Institute of Space Device Engineering. URL: https://www.unavco.org/help/glossary/docs/ICD_GLONASS_5.1_%282008%29_en.pdf.

Russian Space Systems (2011). GLONASS Interface Control Document: Navigational radio signal in the L3 band with open access and code division (edition 1; in Russian). Technical Report Russian Rocket and Space Engineering and Information Systems Corporation, Joint Stock Company.

Russian Space Systems, 2016a. GLONASS Interface Control Document: Code Division Multiple Access Open Service Navigation Signal in L1 frequency band, edition 1.0. Technical Report Russian Rocket and Space Engineering and Information Systems Corporation, Joint Stock Company.

Russian Space Systems, 2016b. GLONASS Interface Control Document: Code Division Multiple Access Open Service Navigation Signal in L2 frequency band, edition 1.0. Technical Report Russian Rocket and Space Engineering and Information Systems Corporation, Joint Stock Company.

Russian Space Systems, 2016c. GLONASS Interface Control Document: Code Division Multiple Access Open Service Navigation Signal in L3 frequency band, edition 1.0. Technical Report Russian Rocket and Space Engineering and Information Systems Corporation, Joint Stock Company.

Russian Space Systems, 2016d. GLONASS Interface Control Document: General Description of Code Division Multiple Access Signal System, edition 1.0. Technical Report Russian Rocket and Space Engineering and Information Systems Corporation, Joint Stock Company.

Simsky, A., 2006. Three's the charm: triple-frequency combinations in future GNSS. InsideGNSS 1 (5), 38–41.

Steigenberger, P., 2023. New birds in the sky: GPS III, GLONASS-K2, NVS-01; GEO-Kolloquium TU Wien, Dec. 18, 2023.

Steigenberger, P., Montenbruck, O., 2022. IGS Satellite Metadata File Description, Version 1.00, December 13, 2022. Technical Report. https://doi.org/10.57677/metadata-sinex.

Steigenberger, P., Montenbruck, O., 2024. Characterization of the GLONASS-K1+ atomic frequency standard. GPS Solut., Submitted.

Steigenberger, P., Montenbruck, O., Hessels, U., 2015. Performance evaluation of the early CNAV navigation message. Navigation 62 (3), 219–228. https://doi.org/10.1002/navi.111.

Strasser, S., Mayer-Gürr, T., Zehentner, N., 2019. Processing of GNSS constellations and ground station networks using the raw observation approach. J. Geod. 93 (7), 1045–1057. https://doi.org/10.1007/s00190-018-1223-2.

Thoelert, S., Steigenberger, P., Montenbruck, O., 2024. GLONASS-K2 signal analysis. GPS Solut. 28 (3), 141. https://doi.org/10.1007/s10291-024-01681-z.

UNAVCO Community, 2004. PBO GPS network – AV09-Haystack__AK2004 P.S., GAGE Facility, GPS/GNSS observations dataset. https://doi.org/10.7283/T5GQ6VP0.

UNAVCO Community, 2006. PBO GPS network – AC67-PillarMtn_AK2006 P.S., GAGE Facility, GPS/GNSS observations dataset. https://doi.org/10.7283/T5Q23X61.

UNAVCO Community, 2007a. PBO GPS network – AB18-Kotzebue__AK2007 P.S., GAGE Facility, GPS/GNSS observations dataset. https://doi.org/10.7283/T51834GZ.

UNAVCO Community, 2007b. PBO GPS network – AB43-CapeSpenceAK2007 P.S., GAGE Facility, GPS/GNSS observations dataset. https://doi.org/10.7283/T5SF2T6T.

UNAVCO Community, 2007c. PBO GPS network – AC74-Cantwello_AK2002 P.S., GAGE Facility, GPS/GNSS observations dataset. https://doi.org/10.7283/T5WW7FPV.

UNAVCO Community, 2007d. SuomiNet-G GPS network – SG27-Barrow SuomiNet P.S., GAGE Facility, GPS/GNSS observations dataset. https://doi.org/10.7283/4SCP-AJ10.

Weiss, J., Steigenberger, P., & Springer, T. (2017). Orbit and clock product generation. In: Teunissen, P., Montenbruck, O. (Eds.), Springer Handbook of Global Navigation Satellite Systems chapter 34, pp. 983–1010. https://doi.org/10.1007/978-3-319-42928-1_34.

Wu, J.-T., Wu, S.C., Hajj, G., et al., 1993. Effects of antenna orientation on GPS carrier phase. Manuscr. Geod. 18 (2), 91–98.